Dynamical Monte Carlo Simulations of 3-D Galactic Systems in Axisymmetric and Triaxial Potentials

Ali Taani[1,3] and Juan C. Vallejo[2]

[1] Applied Science Department, Aqaba University College, Al-Balqa Applied University, P.O. Box 1199, Aqaba, Jordan
[2] European Space Astronomy Centre, PO Box 78, E-28691 Villanueva de la Canada, Madrid, Spain
[3] Email: ali82taani@gmail.com

Abstract

We describe the dynamical behavior of isolated old ($\geq$ 1Gyr) objects-like Neutron Stars (NSs). These objects are evolved under smooth, time-independent, gravitational potentials, axisymmetric and with a triaxial dark halo. We analysed the geometry of the dynamics and applied the Poincaré section for comparing the influence of different birth velocities. The inspection of the maximal asymptotic Lyapunov (λ) exponent shows that dynamical behaviors of the selected orbits are nearly the same as the regular orbits with 2-DOF, both in axisymmetric and triaxial when (ϕ, q_z)= (0,0). Conversely, a few chaotic trajectories are found with a rotated triaxial halo when (ϕ, q_z)= (90, 1.5). The tube orbits preserve direction of their circulation around either the long or short axis as appeared in the triaxial potential, even when every initial condition leads to different orientations. The Poincaré section shows that there are 2-D invariant tori and invariant curves (islands) around stable periodic orbits that bound to the surface of 3-D tori. The regularity of several prototypical orbits offer the means to identify the phase-space regions with localized motions and to determine their environment in different models, because they can occupy significant parts of phase-space depending on the potential. This is of particular importance in Galactic Dynamics.

Keywords: Neutron Stars: general – galaxies: galactic potentials – galaxy: disk – galaxies: kinematics and dynamics – Hamiltonian systems – ordered and chaotic motion – stars: statistics

1 INTRODUCTION

Neutron stars (NSs) manifest the most extreme values of many stellar and physical parameters including spin period, orbital parameters, magnetic field, and kick velocity. These are typically old systems (1–10 Gyr) and relatively short timescales ($\sim 10^6$ yr) (e.g. Yakovlev & Pethick 2004; Lorimer 2008) and show a concentration towards the Galactic centre bulge (which is at ~8 kpc) and in the globular clusters (Caranicolas & Zotos 2009; Taani et al. 2012a; Kalamkar 2013; Taani 2016).

It is generally believed that Millisecond Pulsar (MSPs) are very old NSs spun up owing to mass accretion during the phase of mass exchange in binaries (Alpar et al. 1982). These systems are detectable as active radio pulsars only when they recycled (spun up). While the isolated old NSs have not been identified (Haberl 2007; Kaplan 2008), and we define them here by their steady flux, predominantly thermal X-ray emission, lack of optical or radio counterparts, and the absence of a surrounding pulsar wind nebula (e.g. Ostriker, Rees, & Silk 1970; Shvartsman 1971; Neuhäuser & Trümper 1999;

Treves et al. 2000; Pavlov, Sanwal, & Teter 2004; De Luca 2008; Halpern & Gotthelf 2010) . As a consequence, little is known about their physical and statistical properties. One would hope that the isolated old NSs may be detected as soft X-ray sources (0.5–2 keV) in the *eRosita* all-sky survey (Merloni et al. 2012; Doroshenko et al. 2014). However, the estimation of the pulsar velocities depends on the direct distance measurements (Hobbs et al. 2005) which can be obtained by the dispersion measure and a Galactic density model (Paczyński 1990; Hansen & Phinney 1997; Cordes & Chernoff 1998; Lorimer 2008; Sartore et al. 2010). These studies give a mean birth velocity 100–500 km s^{-1}, with possibly a significant population having $v \geq 1\,000$ km s^{-1}. Arzoumanian, Chernoff, and Cordes (2002) favour a bimodal pulsar velocity distribution, with peaks around 100 and 500 km s^{-1}. However, the mechanisms of high velocity are still open questions (Wang & Han 2010).

Isolated old NSs have attracted much attention because of the hope that their properties could be used to constrain the poorly understood behaviour. Studying their orbital dynamics in known gravitational potential is very significant to

1

our understanding the Galactic gravitational field, as well as the evolution of the Galactic disk structure itself. Paczyński (1990) (hereafter P90) simulated the motion of NSs in a galactic potential and calculated the NS space density distribution. In the same work, P90 also suggested a simplified expression for the gravitational potential which is still often applied in the simulation of NS distribution.

This paper is the third in a series of papers. Wei et al. (2010a, hereafter Paper I) used this potential, and they also adopted a Galactic distribution with one-component initial random velocity models. Wei et al. (2010b) investigated the above gravitational potential of the Galactic disk and several prototypical orbits of stars, and found that all of the orbits are symmetric with respect to the galactic plane. Taani et al. (2012b, hereafter Paper II) constructed a phenomenological model with the same gravitational potential, but under a two-component Maxwellian initial random velocity distribution following P90 and Faucher-Giguère & Kaspi (2006). The conclusion was that there are some non-symmetric orbits. When the motion ranges in the vertical direction and hence becomes larger than the one in the radial direction, the orbits become more regular. It was also found that the irregular character of the motion of NSs increases when the vertical direction becomes larger than radial direction. We mean here when the motion is out of the disk plane. The large Galactic radial expansion (understood as $R \sim 15$ Kpc) could give hints to the distribution of NS progenitors. The majority of them (80%) falls within $R \leq 25$ kpc from the Galactic rotation axis.

In the present paper, we extend and complete the study of the old NS sample by describing the dynamical orbital evolution of the isolated old NSs. These isolated NSs are evolved under a smooth, time-independent, 3-D axisymmetric gravitational potential that represents a non-rotated galactic disk. In addition, we extend the purpose of the present study to explore the orbital dynamics of realistic triaxial potential in a systematic way. We focus on plotting the 3-D trajectories and their 2-D projections under a variety of initial conditions. These initial conditions are obtained by performing Monte Carlo simulations to develop perturbation approximations of the 3-D orbits.

Our main objective is to investigate the regular or chaotic nature of the computed trajectories. It is noteworthy to mention that Evans (1994) found some semi-stochastic orbits in triaxial potentials, because the chaos was tentatively associated with linear instability of the short- and intermediate-axis orbits, while Goodman & Schwarzschild (1981) discussed the importance of stochastic orbits in triaxial models.

The structure of the paper is as follows. First, we introduce the model and the Monte Carlo technique we have used. Then, we will analyse the dynamical properties of a set of selected initial conditions, including the Poincaré sections, Lyapunov Asymptotic Exponents, and dark triaxial haloes case. Finally, we will end with some conclusions.

2 SIMULATION AND NUMERICAL SETUP

2.1. Galactic gravitational potential

The equations presented in this paper describe how could the motion and position of NSs be affected by the Galactic gravitational potential. We will follow papers I and II in their procedures to introduce the P90 Galactic gravitational potential. This model is time independent and very simple. The integration of the orbit, using this model, is very rapid and can achieve high numerical precision.

It is noteworthy to mention here that the P90 model is taken to be a homogeneous function of the density, and ignore the interstellar friction. This is a reliable approximation for our axisymmetric model, because the steady state distribution of old NSs depends only weakly on the non-homogeneous part of the galactic potential (Frei, Huang, & Paczyński 1992). Using P90 may not be a good approximation when studying non-axisymmetric models, because rotating non-axisymmetric components (like bars or spirals) can introduce resonances (Patsis et al. 2002). This model is time independent and very simple. The integration of the orbit, using this model, is very rapid and can achieve high numerical precision. This model combines three axisymmetric potential-density forms to produce a model of the matter distribution and its gravitational potential of the Milky Way. The basic components of the Milky Way are the visible *disk* and *spheroid*, and the invisible dark matter *halo*. For the bulge (spheroid), we adopt a Plummer sphere (Plummer 1911) in order to increase the central mass of the galaxy. For the disk, we adopt Miyamoto–Nagai potential (Miyamoto & Nagai 1975) which is added in order to reproduce the scale length of the disk corresponding to $n = 0$. However, Evans & Bowden (2014) and Evans & Williams (2014) presented new analytical families of axisymmetric dark matter haloes, based on interesting modifications of the Miyamoto–Nagai potential, called Miyamoto–Nagai sequence. And for the dark matter halo, we adopt a logarithmic (modified sphere) potential, which produces a flat rotation curve at large radius, since for strongly flattened systems it is more natural to work in cylindrical coordinates R, z, ϕ rather than spherical r, θ, ϕ (Binney, Merrifield, & Shu 1988; Flynn, Sommer-Larsen, & Christensen 1996).

$$\Phi = \Phi_{\text{sph}} + \Phi_{\text{disk}} + \Phi_{\text{halo}} \qquad (1)$$

where Φ_{sph}, Φ_{halo}, and Φ_{disk} define the spheroid, halo, and disk components, respectively.

The first two components are described by the same law. For the disk component, we follow a Miyamoto–Nagai potential:

$$\Phi_{\text{disk}}(R, z) = -\frac{GM_{\text{disk}}}{\sqrt{R^2 + [A + (z^2 + B^2)^{1/2}]^2}} \qquad (2)$$

where it depends on two variables, namely R, which denotes the radial distance perpendicular to the Galactic central axis, $R^2 = x^2 + y^2$ and z, which denotes the vertical distance from the Galactic plane. The parameter A is a measure of the radial

scale length of the disc while the parameter B is a measure of the disc thickness in the z direction. Galactic discs are much larger in the radial than in the vertical directions, thus the values A will be greater than those of the B parameter in our models. The corresponding values for the disk component are $A = 3.7$ kpc, $B = 0.20$ kpc, and $M_{\text{disk}} = 8.01 \times 10^{10}$ M$_\odot$.

Using Poisson's equation, $\nabla^2 \phi = 4\pi \rho G$, we can obtain the expression for the disc density as

$$\rho(R, z) = \left(\frac{B^2 M}{4\pi} \right) \frac{AR^2 + (A + 3\sqrt{z^2 + B^2})(A + \sqrt{z^2 + B^2})^2}{[R^2 + (A + \sqrt{z^2 + B^2})^2]^{5/2}(\sqrt{z^2 + B^2})^{3/2}} \tag{3}$$

Note that when $A = 0$, the potential reduces to a spherical potential on the galactic plane ($z = 0$). The spheroid component of the Galactic gravitational potential is similar to the above:

$$\Phi_{\text{sph}}(R, z) = -\frac{GM_{\text{sph}}}{\sqrt{R^2 + [A + (z^2 + B^2)^{1/2}]^2}} \tag{4}$$

The spheroid component, $A = 0.0$ kpc, $B = 0.28$ kpc, and $M_{\text{sph}} = 1.12 \times 10^{10}$ M$_\odot$. Here, we must point out, that this potential is not intended to represent a black hole nor any other compact object, but a dense and massive bulge. Therefore, we do not include any relativistic effects (Jung & Zotos 2015).

Regarding the halo component of the Galactic gravitational potential, is given by the following equation:

$$\Phi_{\text{halo}} = \frac{GM_{\text{halo}}}{r_c} \left[\frac{1}{2} \ln \left(1 + \frac{R^2 + z^2}{r_c^2} \right) \right.$$
$$\left. + \frac{r_c}{\sqrt{R^2 + z^2}} \arctan \left(\frac{\sqrt{R^2 + z^2}}{r_c} \right) \right] \tag{5}$$

where $r_{\text{halo}} = 12$ kpc and $M_{\text{halo}} = 5.0 \times 10^{10}$ M$_\odot$.

While in a spherically symmetric potential, the x, y, and z components of the angular momentum and the total angular momentum are conserved, out potential only admits two conserved quantities, the total energy E, and the z-component of the angular momentum vector. Therefore, the motion of the objects are in the plane and perpendicular to the vector of the total angular momentum. We assume that the rotation curve is composed of a spheriod, disk, averaged circular velocity, and triaxial halo components in the Galaxy (see Figure 1), and is calculated at any radius by $v_c^2(r) = r \frac{d\Phi}{dr}$. It is clearly seen from the same figure that each contribution prevails in different distances form the galacto-centric R. In particular, at small distances when $R \geq 3$ kpc, the contribution from the spheriod dominates, while at distances of $3 < R < 19$ kpc the disk contribution is the dominant factor. On the other hand, at large enough galacto-centric distances, $R > 19$ kpc, we see that the contribution from the triaxial halo prevails, thus forcing the rotation curve to remain at with increasing distance from the centre (Zotos 2014).
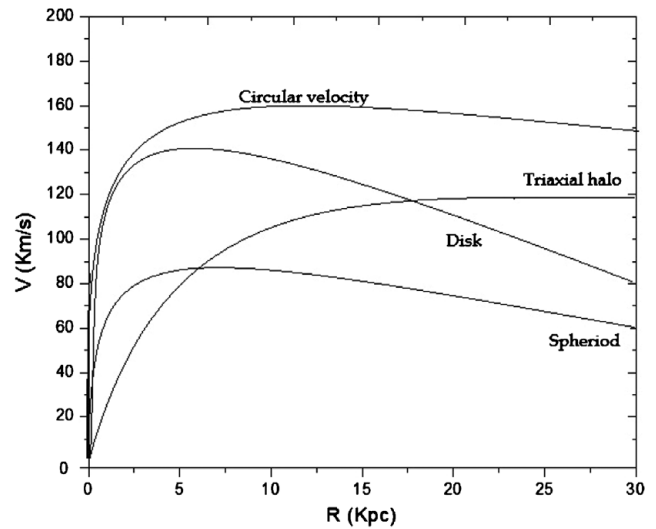
Figure 1. Rotation curve of the axisymmetric potential includes a Miyamoto–Nagai disk and spheriod, triaxial halo, and averaged circular velocity in the galactic plane.

2.2. NS initial velocities

The initial velocities of the NSs are calculated as the vector addition of three different velocities: (1) a Maxwellian distribution, (2) a constant kick, and (3) the circular rotation velocities at the birth place. The details on their calculation can be found in Arzoumanian et al. (2002) and Hobbs et al. (2005) and are summarised here.

Concerning the density distribution of the total number of NSs which we used in this simulation, it is about $\sim 1 \times 10^7$, and it distributes uniformly in the age ≥ 1 Gyr. This is equivalent to a simulating birthrate of one NS per century (Kulkarni & van Kerkwijk 1998; Lyne & smith 2007). However, the precise estimates of both the number and lifetime of the NS population are hard to obtain especially at larger distances (see e.g. Keane & Kramer 2008; Ofek 2009) because they may have been heavily biased by a number of observational selection effects (Lorimer 2008).

Regarding the kicks simulation, the kick velocity imparted to an NS at birth is one of the major problems in the theory of stellar evolution. However, the physical mechanism that causes this kick is presently unknown and a number of physical models have been described and evaluated (see e.g. Kalogera 1996; Wang & Han 2010; Meng, Chen, & Han 2009). But it is presumably the result of some asymmetry in the core collapse or subsequent SNe explosion (see e.g. Pfahl, Rappaport, & Podsiadlowski, 2002; Podsiadlowski et al. 2004). However, the distribution of the kick amplitudes is usually obtained from the analysis of radio pulsar proper motions (Hobbs et al. 2005).

The short-lived sudden kick in the phase space has a kick direction uncorrelated with the orientation of the plane and the system velocity that the object acquires because the explosion is also uncorrelated with the rotation in the Galaxy.

Table 1. Selected representative orbits, θ and Φ in degrees, $|v|$ in km s^{-1}.

Orbit label	Initial position (x_0, y_0, x_0)	Initial position (r_0, θ_0, Φ_0)	Initial velocity (v_{x0}, v_{y0}, v_{z0})	$|v|$
O1	$(-1.11, -9.2, 0.008)$	$(9.267, 0.049, -96.87)$	$(172.4, -53.0, -121.2)$	217.302
O2	$(-2.14, -4.0, 0.1)$	$(4.538, 1.26, -118.14)$	$(15.8, -161.8, -137.4)$	212.856
O3	$(6.88, -6.78, 0.2)$	$(9.661, 1.18, -44.58)$	$(48.5, -44.7, -123.7)$	140.185

Therefore, we follow Hansen & Phinney (1997) and find that the distribution is consistent with Maxwellian distribution of kick velocity. Finally, regarding the third element used in the calculation of the initial condition, we choose the initial circular rotation velocity of the NS before a kick. A plot of averaged circular velocity for every parts of our galactic potential model presented is in Figure 1. It rises linearly up to a maximum value and then they become constant for larger radii.

A distinct approach to the analysis of location and velocity of old NSs is based on the Monte Carlo simulation of the evolution of a simulated sample with different initial parameters, and then their orbits are numerically integrated. We would utilise the method of the Poincaré sections to explore their motions. This has been studied in detail in Papers I and II). Once we have selected the above, we can chose a set of initial conditions. We will consider isolated NSs (excluding the MSPs and GCs), being of ages older than 10^9 yrs and with large radial expansions, $10 > R > 25$ Kpc. The radial distribution has an exponential scale length of $\lambda e^{-\lambda|z|}$, where $\lambda = 1/0.07^\sim$ kpc^{-1}. Here, we assumed a maximum birth height off the plane, z_{max} of 150 pc.

3 NUMERICAL RESULTS

3.1. Selection of initial conditions

We deal in this section with the analysis of the dynamical evolution of a representative set of NSs' Orbits in the Galaxy calculated following the previously described distribution of velocities. We aim to obtain a set of different orbits representing NSs at given distances from the axis. Our method follows Arzoumanian (2002). We start by choosing a randomly selected initial position, with boundaries located at the Galacto-centric distance in the $r \leq 25$ kpc.

The initial velocity components of the NSs are also obtained from a random sample, following the vector addition of the three different velocities described in the previous section: the Maxwellian distribution, the constant kick, and the circular motion velocities at the birth place. The direction of the initial velocity vector is chosen randomly within the geometric shape of the potential. We start from a vector based on the circular velocity. Then we add a random kick, in the form of a local perturbation, with modulus following the Maxwellian distribution (Hansen & Phinney 1997) and direction to the radial direction. Finally, we add the third vector. This is a

velocity vector with a modulus fulfilling a Maxwellian distribution with $\sigma_v = 265$ km s^{-1} (Hobbs et al. 2005; Story & Gonthier 2007) and $\sigma_v = 190$ km s^{-1} (Hansen & Phinney 1997). The direction is given by selecting randomly a direction specified by choosing two angles, $0 < \Phi < 360$ and $-90 < \theta < 90$ (Kiel & Hurly 2009).

The equations above were solved numerically in three directions using the -order Runge–Kutta method with adaptive control step sizes (Press et al. 1992). The initial step size is $dt = 10^{-4}$ Myr, and calculations of position and velocity in 3-D then continue until 0.1 Myr with adjusted step sizes according to the required accuracy. The data are recorded every 0.1 Myr and the total energy $E_{tot} = \frac{1}{2}(v_x^2 + v_y^2 + v_z^2) + \Phi(R, z)$ is checked. The position and velocity then are used for input of the next 0.1 Myr. The procedure used here enabled us to control and achieve required levels of accuracy by using the energy integral.

The Monte Carlo simulations were run and the results are given here. One hundred initial conditions were obtained. Different families are identified and we have selected O1, O2, O3. These orbits are listed in Table 1. A periodic orbit is found when the initial and final coordinates coincide with an accuracy at least 10^{-15}. This is a representative set because they show the typical behaviour of the whole distribution, with very large Galactic radial expansion and they are rosette-like type orbits. In addition, the orbits lie essentially in the plane of the long and intermediate axes and so reinforces the shape of the potential to some extent. The most general trajectory for an object in this potential, which allowed us to clarify properties on the structure and configuration of the invariant tori that we encounter in the vicinity of the periodic orbits. The exact initial conditions for the periodic orbit are calculated and listed in Table 1. The trajectories and 2-D projections corresponding to the integration of every initial condition up to a timescale of 10^8 yr are presented in Figures 2–5.

As we can see from Figure 2, the different initial heights have an influence on z-direction due to the perturbations and will naturally cause different trajectories, while if the objects are located at different R, trajectories can be less different and may prone to instability through the gravitational perturbation.

It is noteworthy to mention here that if the sun received a kick velocity (50 km s^{-1}) in the Galactic plane (Repetto, Davies, & Sigurdsson 2012), the typical orbit (considered as a circular in the Galactic potential) would turn into a rosette orbit.
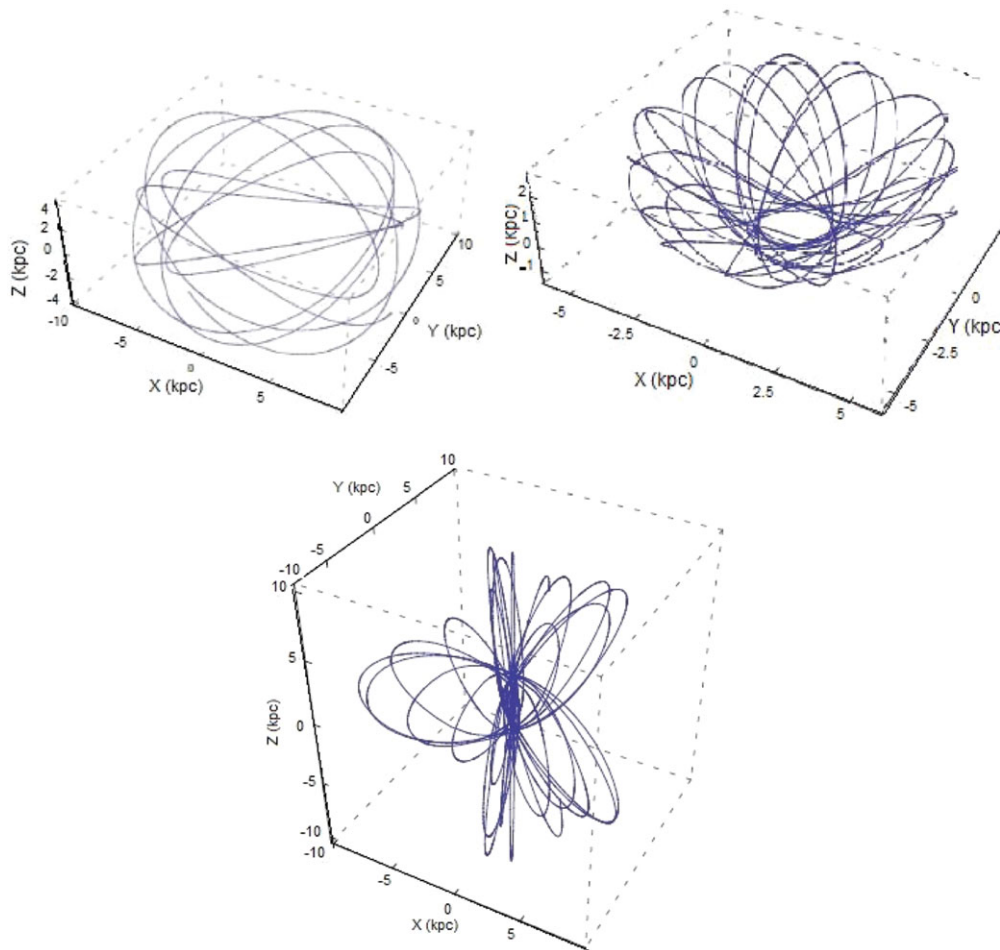
Figure 2. Trajectories corresponding to the different initial conditions of Table 2. These conditions are given in enlarged scale, in order to better view the corresponding morphology. The upper-left panel corresponds to orbit O1. The upper-right panel corresponds to orbit O2. The trajectory is recognised as a precessing banana orbit (see Evans & Bowden 2014). The bottom-left panel corresponds to orbit O3.

3.2. Dynamical analysis

3.2.1. Poincaré sections

In Poincaré sections, periodic orbits appear in the surface of section as a finite set of points. The amount of points depends from the multiplicity of the periodic orbit. This method has been extensively applied to 2-D Hamiltonians in a 2-D plane (Lichtenberg & Lieberman 1992; Wei et al. 2010a; Taani et al. 2012b). While in 3-D systems, we have to project the Poincaré surface to spaces with lower dimensions (Contopoulos 2004).

By setting y, v_{y0} equal to zero at $t = 0$ (remaining zero at all times) in the Hamiltonian equation, the 3-D Poincaré sections can be found in Figure 3. The points in these figures show the 3-D section. We generate 2 500 consequents of the orbits in 3-D (x, v_x, z). We find that there are sometimes several orbits from the same family plotted very close to each other. This happens when the sequence of orbits within the family reverses its progression in the x–z plane towards a given direction and very close to the current space position, causing an accumulation of orbits near this position with different local velocities. The stable periodic orbits are surrounded by

quasi-periodic orbits that bound to the surface of 3-D tori in a 3-D Hamiltonian system. These quasi-periodic orbits are represented in the surface of section by 2-D tori (Manos, Skokos, & Antonopoulos 2012).

Aiming to gain a better picture, Figure 4 shows the 2-D projection in x–z plane, meanwhile Figure 5 shows the 2-D projection in $x - v_x$. In the first figure, the intersection points distribute in some regular lines on the Poincaré hyper-surface section, while the $x - v_x$ projections are tend to have enclosed curves. This behaviour could indicate a regular motion and a quasi-periodic orbit. All the points along the orbits form ensembles of invariant subset of phase space. The ensemble of old NSs along given orbits for invariant blocks of the galaxy, since the galaxies are seen as built not of stars, but of orbits (Guarinos 1992).

3.2.2. Lyapunov asymptotic exponents

We can conclude from the inspection of these figures all orbits seem to be regular orbits, because they are represented by a tori in the surface of sections (Katsanikas & Patsis 2011).
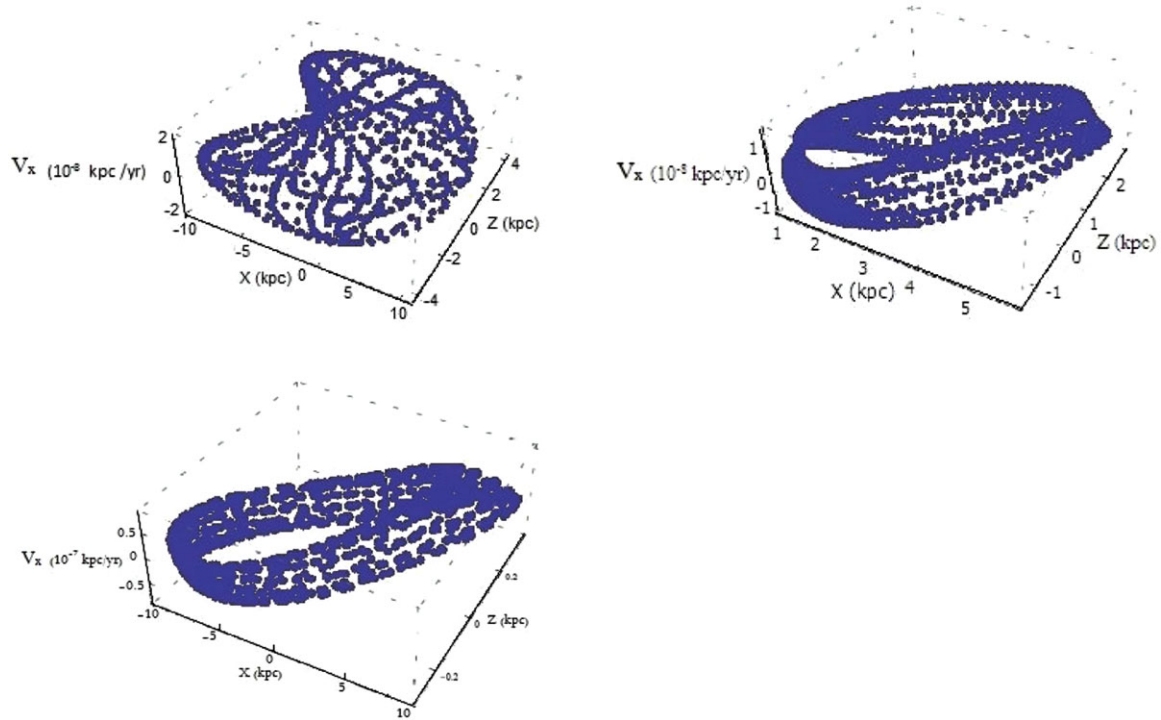
Figure 3. The 3-D Poincaré section $x > 0$, at $y = 0$ of the 3-D trajectories corresponding to the selected initial conditions. The upper-left panel corresponds to orbit O1. The upper-right panel corresponds to orbit O2. The bottom left panel corresponds to orbit O3.

In order to crosscheck the results, we have computed the Lyapunov asymptotic exponent for the selected orbits. The ordinary, or *asymptotic* Lyapunov exponent can be defined as

$$\lambda(\mathbf{x}, \mathbf{v}) = \lim_{t \to \infty} \frac{1}{t} \ln \|D\phi(\mathbf{x}, t)\mathbf{v}\| \qquad (6)$$

provided this limit exists (Ott & Yorke 2008). Here, $\phi(\mathbf{x}, t)$ denotes the solution of the flow equation, such that $\phi(\mathbf{x}_0, 0) = \mathbf{x}_0$, and D is the spatial derivative in the direction of an infinitesimal displacement $\mathbf{v}$.

A system trajectory is chaotic if it shows at least one positive Lyapunov exponent, the movement is confined within certain limited region, and the ω-limit set is not periodic neither composed of equilibrium points (Alligood, Sauer, & Yorke 1996). Conversely, if the maximum asymptotic Lyapunov exponent is zero, this reflects the existence of a regular motion (that is, a quasi-periodic orbit). Finally, a negative value will reflect the existence of one attractor, but this is not possible in a conservative system like the Hamiltonian we are analysing.

The Lyapunov exponents are computed by calculating the growth rate of the orthogonal semi-axes (equivalent to the initial deviation vectors) of one ellipse centred at the initial position as the system evolves. By solving at the same time, the flow equation and the fundamental equation of the flow (that is, the distortion tensor evolution), we can follow the evolution of the vectors, or axes, along the trajectory, and in turn, their growth rate. This method is described in Benettin et al. (1980).

The selection of the initial deviation vectors is of importance when computing the Lyapunov exponents during finite integrations, leading to the so-called finite-time Lyapunov exponents (Vallejo, Aguirre, & Sanjuan 2003). But when one uses long enough integration times, the axes evolve towards the fastest growing direction and the computation of the growth rates return the asymptotic Lyapunov values (Vallejo, Viana, & Sanjuan 2008).

We have used integration of up $T = 10^5$ time-units and the resulting maximal Lyapunov values have been nearly zero in all cases, confirming the analysis done using the Poincaré section methods, it is seen that all orbits retain their regular characteristics along the stellar evolution, the regular orbit bound to the surface of 3-D torus (Kovár et al. 2013) in the phase space forms a narrow curve with zero width. This may be due to a different kick velocities due to SNe mass-loss and natal kicks to the newly formed NS (Podsiadlowski et al. 2004). By examining the Poincaré section in each case, we found that the system looks integrable and its trajectories lie mostly on tori. These tori are represented by 2-D tori in the surface of section. This is known the KAM (Kolmogorov–Arnold–Moser) theorem (Kolmogorov 1954; Moser 1962; Arnold 1963).

3.3. Orbits in the dark triaxial halo case

To investigate the possible effects of spiral structure on the orbital characteristics of trajectory and projections, we adopt the triaxial model of Law, Majewski, & Johnston (2009), that
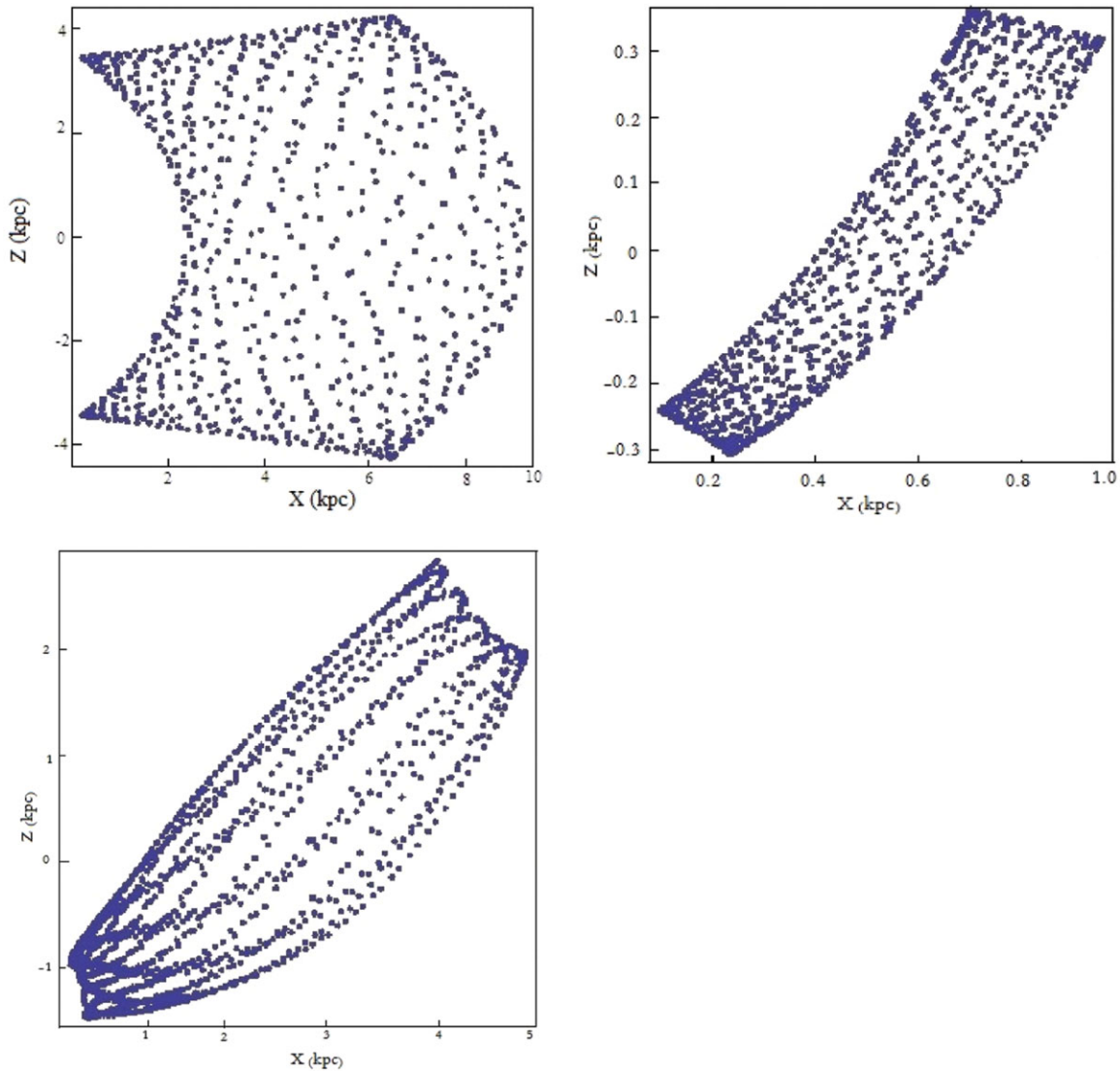
Figure 4. The projection on *x*–*z* plane of the 3-D Poincaré section. The upper left panel corresponds to orbit O1. The upper right panel corresponds to orbit O2. The bottom left panel corresponds to orbit O3.

uses a triaxial halo as follows:

$$\Phi_{\text{halo}} = v_{\text{halo}}^2 \ln(C_1 x^2 + C_2 y^2 + C_3 xy + (\frac{z}{q_z})^2 + r_{\text{halo}}^2) \qquad (7)$$

where $v_{\text{halo}} = 128$ km s^{-1}, q_z represents the flattening perpendicular to the Galactic plane. The various constants C_1, C_2, and C_3 are given by

$$C_1 = \left(\frac{\cos^2 \phi}{q_1^2} + \frac{\sin^2 \phi}{q_2^2} \right) \qquad (8)$$

$$C_2 = \left(\frac{\cos^2 \phi}{q_2^2} + \frac{\sin^2 \phi}{q_1^2} \right) \qquad (9)$$

$$C_1 = 2 \sin \phi \cos \phi \left(\frac{1}{q_1^2} - \frac{1}{q_2^2} \right) \qquad (10)$$

The control parameters of this model are the orientation of the major axis of the triaxial halo ϕ and its flattening q_z. (A detailed discussion on the effects of dark haloes and their role in the dynamics of the galaxies is presented in Vallejo & Sanjaun 2015 and references there.)

This potential is triaxial, rotated, and more realistic. As consequent, it reproduces the flat rotation curve for a Milky Way-type galaxy and it can be easily shaped to the axial ratios of the ellipsoidal isopotential surfaces (see Vallejo & Sanjuan 2015 for details). We include computations of the three orbits correspondence to O1, O2, and O3 which can be found in realistic galactic-type potentials that incorporates spiral arms (see Figures 6 and 7). The main parameters to play with are the flattening (q_z) and the orientation (ϕ) of the dark halo, since the efficiency of bar formation depends very strongly on the initial orientation of the galaxy disk (Lokas et al. 2015). A lot of work on periodic orbits in the plane of a rotating barred galaxy was carried out by Contopoulos & Papayannopoulos (1980), Papayannopoulos & Petrou (1983), Mulder & Hooimeyer (1984), Harsoula et al. (2011a,
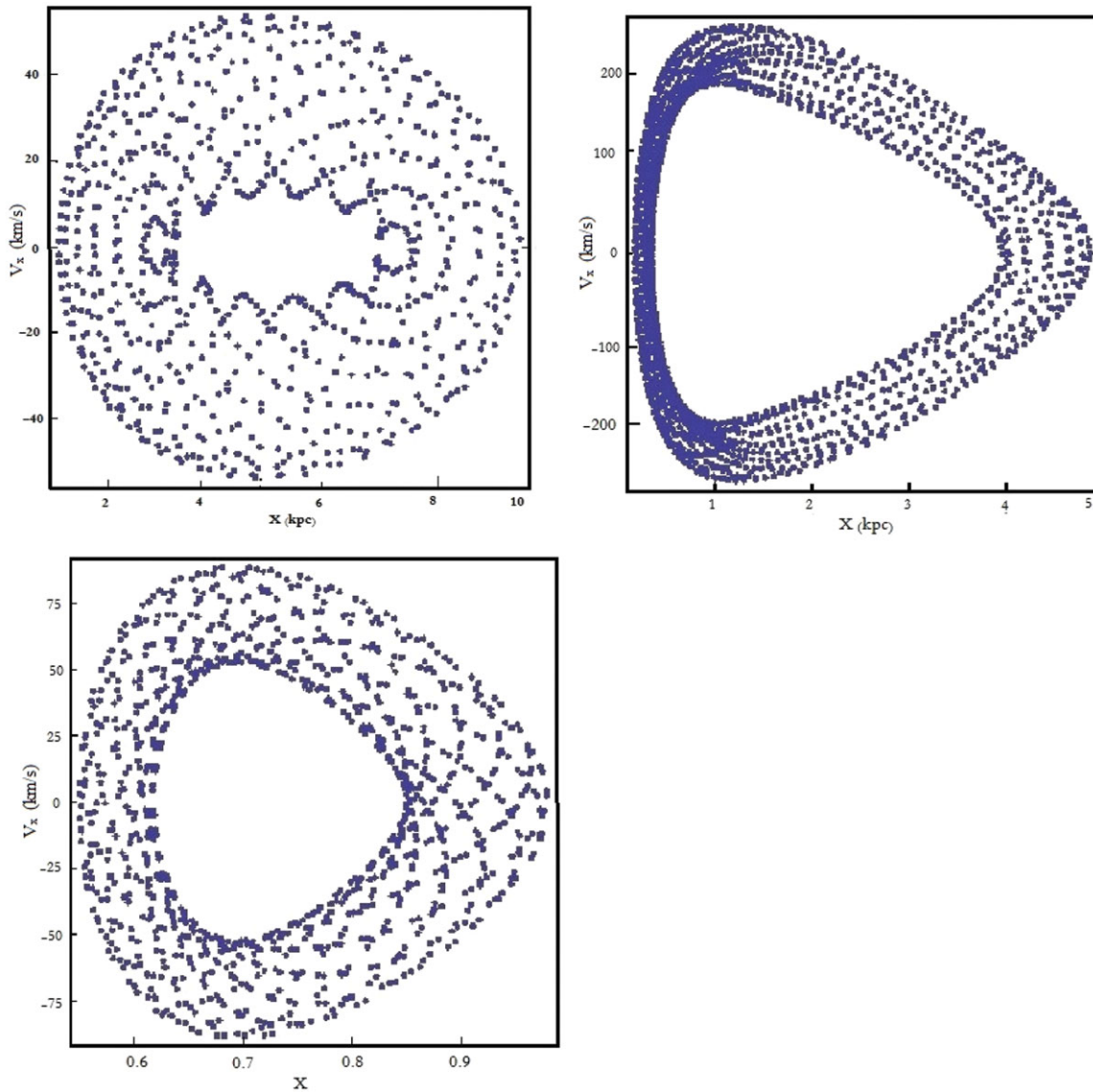
Figure 5. The projection on x–v_x plane of the 3-D Poincaré section. The upper-left panel corresponds to orbit O1. The upper-right panel corresponds to orbit O2. The bottom left panel corresponds to orbit O3.

2011b), and Zotos (2014). All integrable triaxial potentials have a similar orbital structure (e.g. de Zeeuw 1985; Valluri & Merritt 1998; Skokos 2001; Contopoulos 2004; Patsis et al. 2009; Zotos & Carpintero 2013; Patsis et al. 2014). The plots we delivered were done in spherical coordinates by two different values of the dark halo orientation ($\phi = 0$ and $\phi = 90$). Figures 6 and 7 ($\phi = 0$, $q_z = 1.25$, and λ relatively small value and close to zero for O1) show regular orbits (tube orbits with short and long axes) for oblate and prolate cases, respectively. The effect of spiral structure is presented for all orbits and seems to be chaotic regions on the Poincaré sections ($\phi = 90$, $q_z = 1.5$, and $\lambda \geq 1$ for O2 and O3 in Figures 6 and 7). Thus, NSs in this potential follow harmonic and rotating motion in each of the x, y, z directions independently. These control parameter values are given in Table 2 for all orbits. In Figures 6 and 7 (O1), when $\phi = 0$

Table 2. Maximum asymptotic Lyapunov exponents for the selected representative orbits, two different orientations of dark halo.

Orbit label	$\lambda(\phi = 0)$	$\lambda(\phi = 90)$
O1	0.00015160387	0.00015288824
O2	4.5184949	4.3155085
O3	1.9746514	2.0018652

(stationary) q_1 is then aligned at stable equilibrium point with the Galactic x-axis, and the motion is stable along its axis. The results in this case are comparable with non-triaxial, purely logarithmic potentials. When $\phi = 90$, q_1 (see Figures 6 and 7 for O2 and O3) is then aligned with the Galactic y-axis and
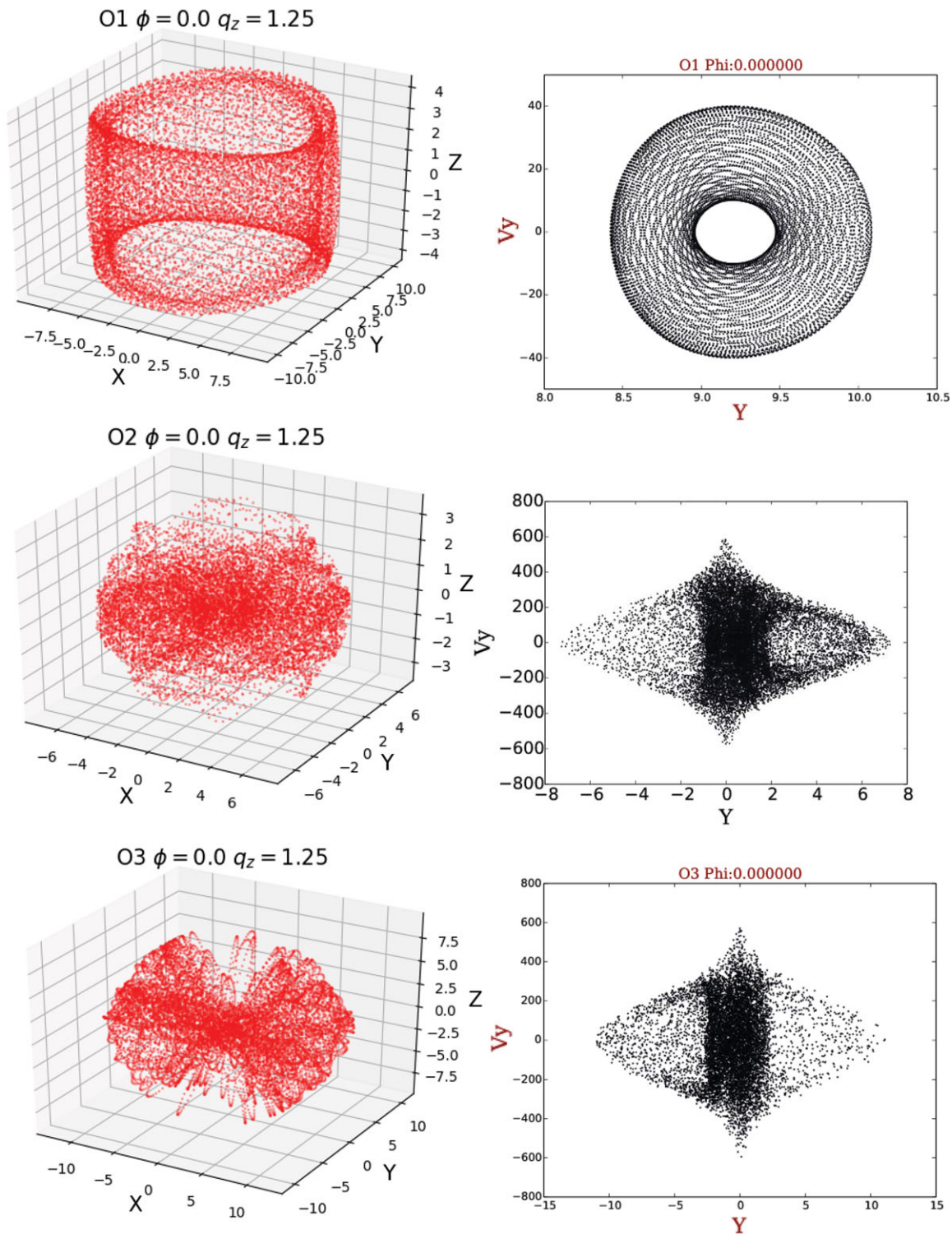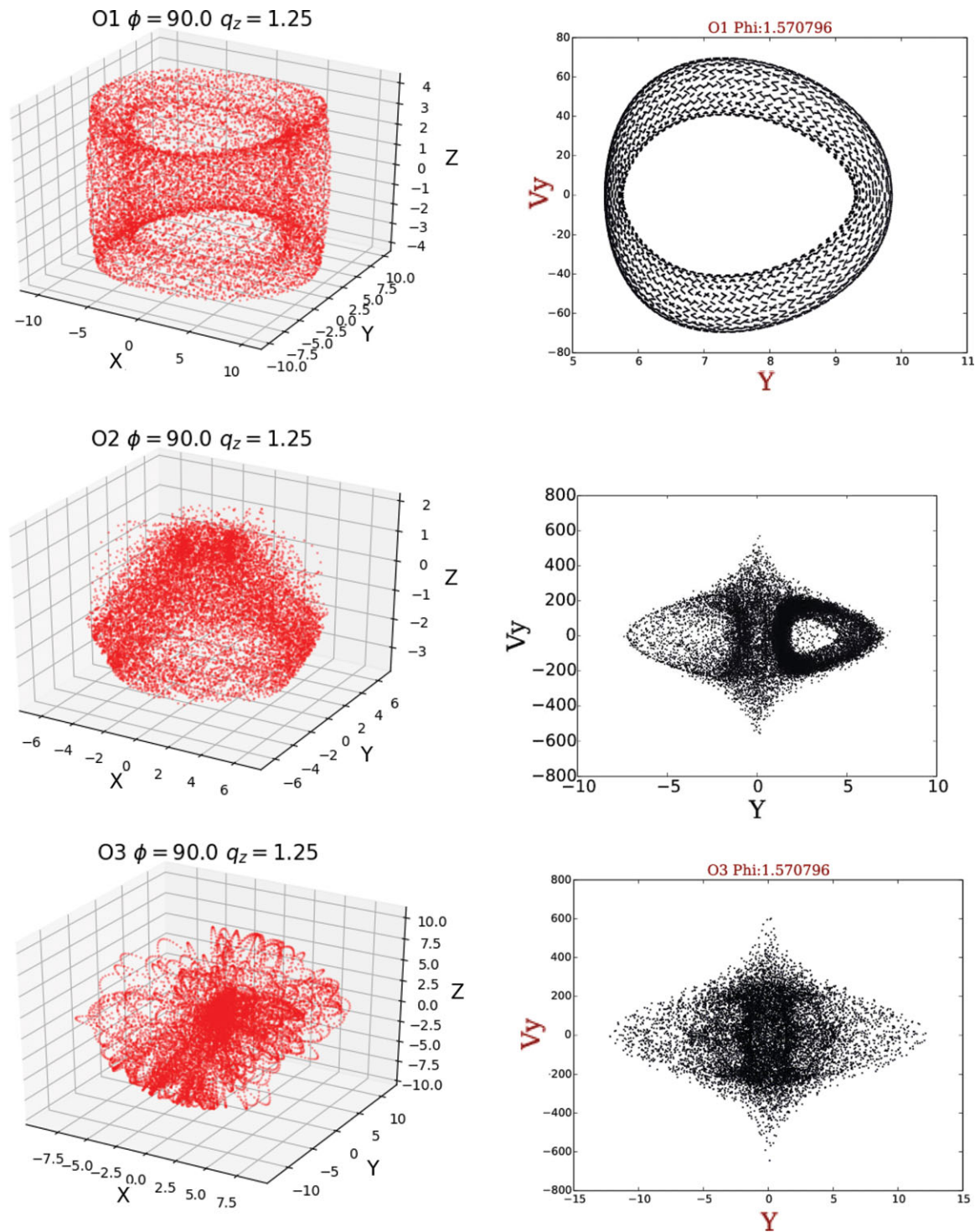
Figure 6. Physical trajectories and the corresponding Poincaré sections y–v_y, with plane $x = 0$ and $v_x > 0$, for the selected representative orbits, for a dark halo orientation of $\phi = 0$.

it takes the role of q_2. We note that tube tori appear in the 3-D projections of the spaces of section as soon as a perturbation is introduced, even if it is a small one (Katsanikas & Patsis 2011). At $(\phi, q_z) = (0, 1.25)$ the outer long-axis tube

in Figure 6 is wider in the x direction than Figure 7 when seen in projection. It is noteworthy to mention that Figure 6 is symmetric in the v_y–y plane, while Figure 7 is not due to the Coriolis force (Gajda, Lokas, & Athanassoula 2016).

Figure 7. Physical trajectories and the corresponding Poincaré sections y–v_y, with plane $x = 0$ and $v_x > 0$, for the selected representative orbits, for a dark halo orientation of $\phi = 90$.

4 CONCLUSIONS

We have found many interesting aspects for simulation of several prototypical orbits of isolated old NSs and their connections with the spatial distribution phenomena, through the long-term stellar dynamics. We employed 3-D Galactic grav-

itational potential models of normal non-barred galaxies. The models consist of axisymmetric and a triaxial dark halo potentials with three components: bulge, disc, and dark halo. These are relatively simple potentials that can show complex behaviours, which are found in more realistic galactic-type potentials. Then we found that orbits can rotate around the

axis of symmetry of the phase space on a surface of section, in the same direction in 3-D and 2-D loops for various values of the initial conditions for the family of axisymmetric and triaxial models. We have used the Poincaré technique to study the 3-D NS trajectories and their 2-D projections. It is shown that both loop and family of orbits arise as a natural consequence of the dynamics of the stable periodic orbits (with regular motion). In addition, the morphology of orbits in triaxial potentials can determine the structure of triaxial galaxy itself. There are 3-D invariant tori containing quasi-periodic motions, these tori are represented by 2-D tori on the surface of the section associated with phase space. In addition, the Lyapunov asymptotic exponent is equal to zero in case of non-triaxial. However, it is clear that the chaotic orbit have a non-zero real exponent, since the finite-time Lyapunov exponents distributions reflect the underlying dynamics (Vallejo et al. 2003). We also show that the phase space in triaxial galaxies with a rotated halo is rich in regular and chaotic regions, which is consistent with the analysis done by the Poincaré cross-sections. The results of these motions are strongly affected by the gravitational potential of the galactic disk associated with the effect of kick velocities on the orbital parameters. This can provide us a better visualisation of the old NS dynamics.

The conclusions of the present research are considered as an initial effort and also as a promising step in the task of understanding the underlying dynamics of the phase space by mapping the regular regimes in 3-D axisymmetric potential. Future work will go steps further in detection of the old NSs via accretion of the interstellar medium material which may make them shine, and their weak luminosity could be detected as soft X-ray sources (0.5–2 keV). However, *eROSITA* all-sky survey have an excellent capabilities of available survey for this kind of studies, and it should improve our knowledge of Galactic NSs phenomenally for the next decade. *eROSITA* will be about 20 times more sensitive than the ROSAT all sky survey in the soft X-ray band (Merloni et al. 2012).

ACKNOWLEDGEMENTS

REFERENCES

Alligood, K., Sauer, T. D., & Yorke, J. A. 1996, Chaos: An Introduction to Dynamical Systems (New York: Springer-Verlag)

Alpar, M. A., et al. 1982, Nature, 300, 728

Arnold, V. I. 1963, RuMaS, 18, 5

Arzoumanian, Z., Chernoff, D. F., & Cordes, J. M. 2002, ApJ, 568, 289

Benettin, G., et al. 1980, Mecc, 15, 9

Binney, J., Merrifield, S., & Shu, F. 1988, Nature, 333, 219

Caldwell, J., & Ostriker, J. 1981, ApJ, 251, 61

Caranicolas, N. D., & Zotos, E. E. 2009, BaltA, 18, 205

Caranicolas, N. D., & Zotos, E. E. 2013, PASA, 30, 49

Chen, B., et al. 2001, ApJ, 553, 184

Contopoulos, G., & Papayannopoulos, T. 1980, A&A, 92, 33

Contopoulos, G. 2004, Order and Chaos in Dynamical Astronomy (New York: Springer)

Cordes, J. M., & Chernoff, D. F. 1998, ApJ, 505, 315

de Zeeuw, T. 1985, MNRAS, 216, 273

Doroshenko, V., Ducci, L., Santangelo, A., & Sasaki, M. 2014, A&A, 567, 7

Evans, N. W. 1994, MNRAS, 267, 333

Evans, N. W., & Bowden, A. 2014, MNRAS, 443, 2

Evans, N. W., & Williams, A. A. 2014, MNRAS, 443, 791

Faucher-Giguère, C.-A., & Kaspi, V. M. 2006, ApJ, 643, 332

Flynn, C., Sommer-Larsen, J., & Christensen, P. R. 1996, MNRAS, 281, 1027

Frei, Z., Huang, X., & Paczyński, B. 1992 ApJ, 643, 332

Fryer, C., Benz, W., Herant, M., & Stirling, C. A. 1999, ApJ, 516, 892

Haberl, F. 2007, Ap&SS, 308, 181

Halpern, J. P., & Gotthelf, E. V. 2010, ApJ, 709, 436

Hansen, B. M. S., & Phinney, E. S. 1997, MNRAS, 291, 569

Harsoula, M., Kalapotharakos, C., & Contopoulos, G. 2011a, IJBC, 21, 2221

Harsoula, M., Kalapotharakos, C., & Contopoulos, G. 2011b, MNRAS, 2411, 1111

Hobbs, G., Lorimer, D. R., Lyne, A. G., & Kramer, M. 2005, MNRAS, 360, 974

Jung, Ch., & Zotos, E. E. 2015, MeReC, 69, 45

Gajda, G., Lokas, E., & Athanassoula, E. 2016, ApJ, 830, 108

Goodman, J., & Schwarzschild, M. 1981, ApJ, 245, 1087

Guarinos, J. 1992, Evolution of Interstellar Matter and Dynamics of Galaxies (Cambridge: Cambridge University Press)

Kalamkar, M. N. 2013, PhD dissertation, University of Amsterdam

Kalogera, V. 1996, ApJ, 471, 352

Kaplan, D. L. 2008, in AIP Conf. Ser., Vol. 983, 40 Years of Pulsars: Millisecond Pulsars, Magnetars and More (College Park: American Institute of Physics), 331

Katsanikas, M., Patsis, P. A., & Contopoulos, G. 2013, IJBC, 23, 1330005

Keane, E. F., & Kramer, M. 2008, MNRAS, 391, 2009

Kolmogorov, A. 1954, Dokl. Akad. Nuak. SSSR, 98, 527

Kovár, J., Kopácek, O., Karas, V., & Kojima, Y. 2013, QGra, 30, 025010

Kulkarni, S. R., & van Kerkwijk, M. H. 1998, ApJ, 507, L49

Law, D. R., Majewski, S. R., & Johnston, K. V. 2009, ApJ, 703, L67

Lichtenberg, A. J., & Lieberman, M. A. 1992, Regular and Chaotic Dynamics (New York: Springer-Verlag)

Lokas, E. L., Semczuk, M., Gajda, G., & D'Onghia, E. 2015, ApJ, 810, 100

Lorimer, D. R. 2008, LRR, 11, 8 http://relativity.livingreviews.org/Articles/lrr-2008-8/

Lyne, A. G., & Graham-Smith, F. 2007, Pulsar Astronomy, Cambridge Astrophysics Series (3rd edn.; Cambridge: Cambridge University Press)

Manos, T., & Athanassoula, E. 2011, MNRAS, 415, 629

Manos, T., & Machado, R. E. G. 2014, MNRAS, 438, 2201
Manos, T., Skokos, Ch., & Antonopoulos, Ch. 2012, IJBC, 22, 9
Meng, X., Chen, X., & Han, Z. 2009, MNRAS, 395, 2103
Merloni, A., et al. 2012, eprint, arXiv:1209.3114
Miyamoto, M., & Nagai, R. 1975, PASJ, 27, 533
Moser, J. K. 1962, Nachr. Akad. Wiss. Götingen, Math. Phys. K1. IIa, 1
Mulder, W. A., & Hooimeyer, J. R. A. 1984, A&A, 134, 158
Neuhäuser, R., & Trümper, J. E. 1999, A&A, 343, 151
Ofek, E. O. 2009, PASP, 121, 814
Ostriker, J. P., Rees, M. J., & Silk, J. 1970, ApJ, 6, 179
Ott, W., & Yorke, J. A. 2008, PhRvE, 78, 056203
Paczyński, B. 1990, ApJ, 348, 485
Papayannopoulos, T., & Petrou, M. 1983, A&A, 119, 21
Patsis, P. A., Kaufmann, D. A., Gottesman, S. T., & Boonyasait, V. 2009, MNRAS, 394, 142
Patsis, P. A., & Kalapotharakos, C. 2011, MSAIS, 18, 83
Patsis, P. A., & Katsanikas, M. 2014, MNRAS, 445, 3525
Patsis, P. A., et al. 2002, MNRAS, 355, 1049
Pavlov, G. G., Sanwal, D., & Teter, M. A. 2004, in IAU Symp. 218, Young Neutron Stars and their Environments, ed. F. Camilo & B. M. Gaensler (San Francisco: ASP), 239
Perets, H. B., et al. 2009, ApJ, 697, 2097
Pfahl, E., Rappaport, S., & Podsiadlowski, P. 2002, ApJ, 573, 283
Podsiadlowski, Ph., et al. 2004, ApJ, 612, 1044
Press, W. H., et al. 1992, Numerical Recipes (2nd edn.; Cambridge: Cambridge University Press)

Repetto, S. 2012, Master's thesis, Lund Observatory
Repetto, S., Davies, M., & Sigurdsson, S. 2012, MNRAS, 425, 2799
Popov, S. B. 2008, PPN, 39, 1136
Sartore, N., Ripamonti, E., Treves, A., & Turolla, R. 2010, A&A, 510, A23
Shvartsman, V. G. 1971, SvA, 14, 662
Skokos, Ch. 2010, LNP, 790, 63
Skokos, Ch., Antonopoulos, Ch., & Bountis, T. C. 2004, JPhA, 37, 6269
Sun, X. H., & Han, J. L. 2004, MNRAS, 350, 232
Story, S. A., & Gonthier, P. L. 2007, ApJ, 671, 713
Taani, A. 2016, RAA, 16, 1
Taani, A., et al. 2012a, AN, 333, 53
Taani, A., et al. 2012b, Ap&SS, 341, 601
Tabor, M. 1989, Chaos and Integrability in Nonlinear Dynamics (New York: Wiley)
Taylor, J. H., & Cordes, J. M. 1997, ApJ, 411, 674
Treves, A., Turolla, R., Zane, S., & Colpi, M. 2000, PASP, 112, 297
Vallejo, J. C., Aguirre, J., & Sanjuan, M. A. F. 2003, PhLA, 311, 26
Vallejo, J. C., Viana, R., & Sanjuan, M. A. F. 2008, PhLE, 78, 66204
Vallejo, J. C., & Sanjaun, M. A. F. 2015, MNRAS, 447, 3797
Wang, B., & Han, Z. 2010, Ap&SS, 329, 293
Wei, Y. C., et al. 2010a, ChPhL, 27, 9801
Wei, Y. C., et al. 2010b, ScChA, 53, 1939
Yakovlev, D. G., & Pethick, C. J. 2004, ARA&A, 42, 169
Zotos, E. E. 2014, BaltA, 23, 37
Zotos, E. E., & Carpintero, D. D. 2013, CeMDA, 116, 417